Title

Contribution of Sub-Gap States to Broadband Infrared Response in Organic Bulk Heterojunctions

Journal

ACS Applied Materials & Interfaces, 14(47)

ISSN

1944-8244

Authors

Li, Ning
Park, Insun
Vella, Jarrett H
et al.

Publication Date

2022-11-30

DOI

10.1021/acsami.2c17477

Peer reviewed

ACS APPLIED MATERIALS & INTERFACES

www.acsami.org Research Article

Contribution of Sub-Gap States to Broadband Infrared Response in Organic Bulk Heterojunctions

Ning Li, Insun Park, Jarrett H. Vella, Soong Ju Oh, Jason D. Azoulay, Dong-Seok Leem, and Tse Nga Ng*

Cite This: https://doi.org/10.1021/acsami.2c17477 Read Online

ACCESS | Metrics & More | Article Recommendations | Supporting Information

ABSTRACT: This work studied a series of infrared detectors comprised of organic bulk heterojunctions to explain the origin of their broadband spectral response from the visible to the infrared spanning 1 to 8 μm and the transition from photonic to bolometric operation. Through comparisons of the detector current and the sub-bandgap density of states, the mid- and long-wave infrared response was attributed to charge trap-and-release processes that impact thermal charge generation and the activation energy of charge mobility. We further demonstrate how the sub-bandgap characteristics, mobility activation energy, and effective bandgap are key design parameters for controlling the device temperature coefficient of resistance, which reached up to −7%/K, better than other thin-film materials such as amorphous silicon and vanadium oxide.

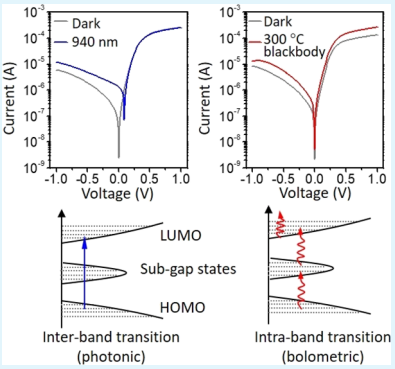

KEYWORDS: *organic semiconductors, infrared detectors, bulk heterojunction, sub-bandgap states, temperature coefficient of resistance*

INTRODUCTION

Uncooled infrared (IR) sensors are essential for myriad applications including biological imaging, security, and industrial processes; however, current technologies require complex fabrication that precludes low-cost, large-area integration.[1] The rapid progress of solution-processed organic semiconductors holds great promise for IR sensing due to advantages associated with facile fabrication, large-area processability, and mechanical flexibility.[2−6] The spectral range of organic detectors has been demonstrated to cover parts of shortwave infrared (SWIR, wavelength λ = 1−3 μm) in photodiodes[7−10] and mid- to long-wave infrared (MWIR, λ = 3−5 μm; LWIR, λ = 8−14 μm) in thin-film resistors.[11−13] Often, the organic semiconductors selected for visible to SWIR detection are thought of as a separate category of materials that are distinct from doped conductive polymers used for temperature-sensing functions, namely, LWIR detection. However, to present a more cohesive view that connects these material systems, this work demonstrates key, interrelated features in narrow-bandgap polymers that bridge these boundaries and offer broadband response from the SWIR to LWIR, with a transition from photonic to thermal detection mechanisms.

The operating mechanisms of IR detectors are diverse; for example, the device response to SWIR light is typically based on photovoltaic[14] or photoconductive[15,16] effects, while the transduction of MWIR−LWIR light includes bolometric,[13,17,18] thermoelectric,[19−21] and pyroelectric effects.[12,22] Thin-film materials such as vanadium oxide[14] and amorphous silicon[23] have been incorporated into bolometric structures in commercial systems with temperature coefficients of resistance (TCR) of −6.7%/K for single-crystal VO_2[24] and −1.8 to −5.5%/K for amorphous silicon (a-Si).[25] Like a-Si, organic semiconductors show thermally activated hopping transport, which makes them inherently sensitive to temperature changes. While thermal sensors based on organic semiconductors are emerging,[12,13,26−28] an in-depth explanation of the origins of the long-wavelength (MWIR−LWIR) response remains nascent. This work demonstrates that it is not sufficient to simply attribute bolometric effects only to the temperature-dependent mobility. Through impedance spectroscopy measurements and better accounting, another contribution to the bolometric response is uncovered and attributed to sub-bandgap trap states that affect thermal generation and in turn the device TCR.

Here, we devote efforts to interpret the photonic and thermal/bolometric responses in a series of organic bulk heterojunction (BHJ) photodiodes. The variety of BHJ compositions leads to different TCRs and allows us to

Received: September 27, 2022
Accepted: November 6, 2022

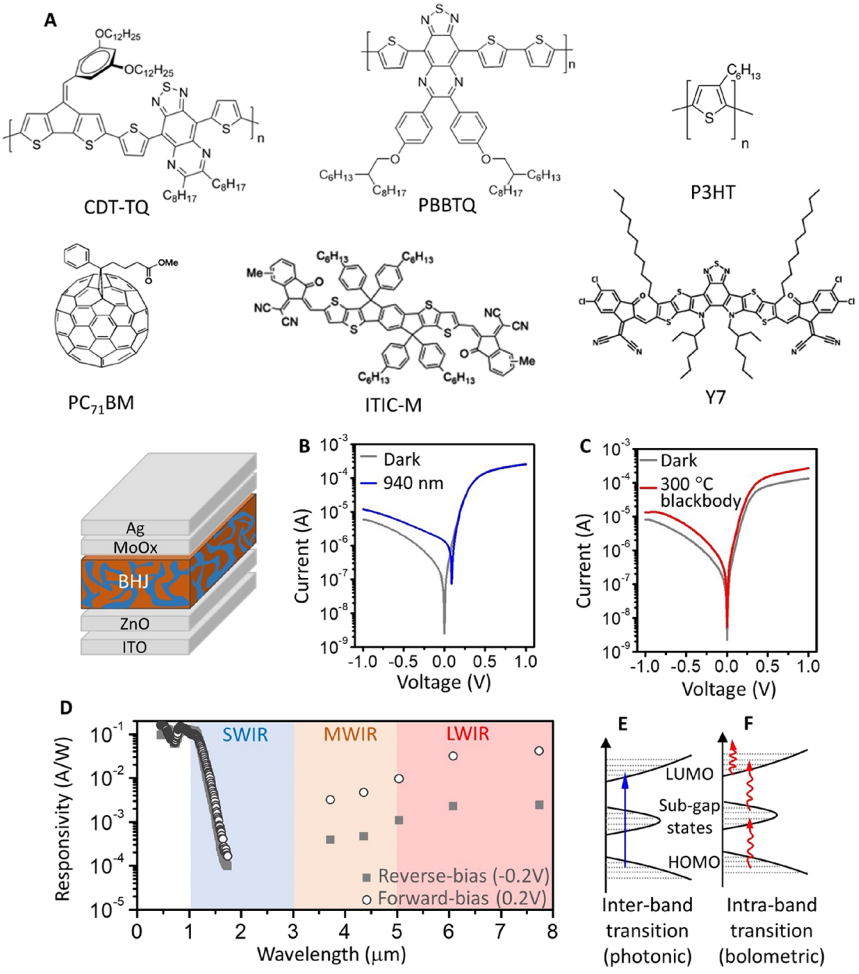

Figure 1. Response of a typical organic photodiode to near- and mid-wave IR radiation. (A) Chemical structures of the materials and a schematic of the detector structure. Current−voltage characteristics under (B) 940 nm light at 0.4 mW/cm^2 and (C) 300 °C blackbody radiation at 3.5 mW/cm^2 with a peak wavelength of 5 μm. Filters were used to block out visible light. Here, the BHJ was based on a CDT-TQ:$PC_{71}BM$ heterojunction at room temperature. (D) Responsivity as a function of wavelength at different biases. The incident light was modulated at 315 Hz for λ < 1.7 μm and at 5.6 mHz for λ > 3 μm. The light intensity is 0.5−1.5 mW/cm^2 for the visible to shortwave IR range and 2−5 mW/cm^2 for the 3−8 μm IR range. Illustrations of (E) inter- and (F) intra-band transitions to distinguish two operational regimes.

correlate performance to three key parameters of charge activation energy, effective energy gap, and the distribution of sub-bandgap states. The study details the mechanism that adjusting the sub-bandgap characteristics can change the detector TCR by up to 7-fold. In addition, the response speeds are characterized to distinguish signals due to SWIR and MWIR/LWIR radiation. While this work focuses on understanding material properties in lieu of optimizing device geometries, the TCR of the organic-based devices reported here is compelling for room-temperature operation, surpassing the values typically exhibited by vanadium oxide or a-Si in commercial bolometric detectors. These findings reveal the significant influence of the sub-bandgap density of states (DOS) on the device sensitivity, thereby providing insight into what DOS characteristics are conducive to high performance and critical for the development of broadband IR detectors.

RESULTS AND DISCUSSION

Different Operational Mechanisms under SWIR and MWIR/LWIR. The organic IR detectors were fabricated as diode structures. The BHJ layers were binary blends of donor polymers and acceptor molecules, and the molecular structures and acronyms are presented in Figure 1A, with the full chemical nomenclatures presented in Figure S1. The donor materials included two narrow-bandgap polymers[29,30] (CDT-TQ and PBBTQ) and a polythiophene (P3HT), and the acceptors included a fullerene derivative ($PC_{71}BM$) and non-fullerene molecules (ITIC-M and Y7). The compositions of the five BHJ combinations studied in this work are listed in Table 1.

Table 1. Compositions of BHJ Films

BHJ type	solvent	concentration (mg/mL)	addictive (w/w, weight ratio; v/v, volume ratio)	thickness (nm)
CDT-TQ:$PC_{71}BM$	DCB	8 + 16	15% camphor (w/w), 3% DIO (v/v)	180
CDT-TQ:ITIC-M	DCB	10 + 10	15% camphor (w/w)	189
PBBTQ:Y7	DCB	15 + 25	1% CN (v/v)	160
PBBTQ:$PC_{71}BM$	DCB	10 + 20	1% DIO (v/v)	170
P3HT:$PC_{71}BM$	DCB	15 + 15	1% DIO (v/v)	150

https://doi.org/10.1021/acsami.2c17477
ACS Appl. Mater. Interfaces XXXX, XXX, XXX−XXX

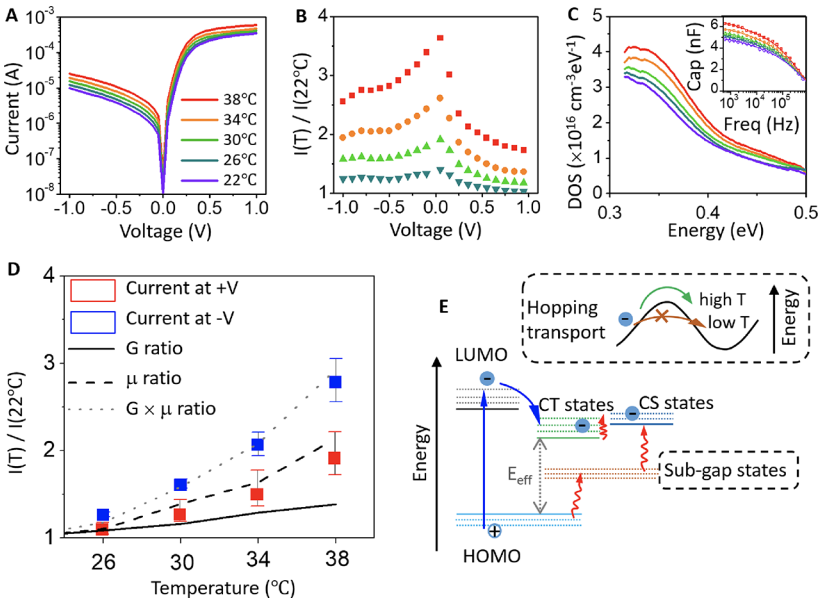

Figure 2. Photodiode characteristics as a function of the device temperature. The BHJ was CDT-TQ:$PC_{71}BM$. The same color legend applies to parts A through C. (A) Current versus voltage. (B) Data in part A normalized to the data taken at 22 °C. (C) DOS versus energy from HOMO band edge. The inset shows the capacitance−frequency characteristics from which DOS were extracted from. (D) Current ratios from part B versus temperature. The square points represent the current ratio data at forward (red) and reverse (blue) biases. The lines are calculated ratios based on generation rate G (eq 2, solid black line), mobility μ (extracted from space-charge-limited current model, dashed black line), and their product (dotted gray line). All ratios were normalized to the values obtained at 22 °C. (E) Illustration showing charge generation through charge-transfer (CT) states (photonic response) and sub-gap states (thermal response) that move carriers to charge-separation (CS) states.[39] The blue straight arrow indicates direct band transition upon photon absorption, while the red curvy arrows represent thermally activated transitions. The zoomed-in box shows thermally activated hopping transport in the conduction band.

The exemplar characteristics in Figure 1B,C were taken on a device with a BHJ comprised of CDT-TQ:$PC_{71}BM$ to compare the response under illumination from a 940 nm light-emitting diode (LED) and from a 300 °C blackbody radiator, respectively. The blackbody radiator was a MWIR−LWIR light source with peak emission wavelength tunable by the body temperature (Figure S2). The measurement under 940 nm light showed a prominent increase in photocurrent at reverse bias and an open-circuit voltage (V_{oc}) associated with the photovoltaic effect. In contrast, under the 300 °C blackbody radiator with a peak emission of 5 μm, the device displayed current increases in both forward and reverse biases and no V_{oc}. Such different behaviors indicated that the detection mechanisms changed between near-IR and MWIR/LWIR spectral regions.

To identify the transition point when operational mechanisms changed, the detector responsivity was measured as a function of the incident wavelength from 0.4 to 8 μm, as shown in Figure 1D. The responsivity was ∼0.1 A/W for λ < 1.1 μm and decreased gradually with a longer wavelength out to 1.7 μm in the SWIR region. Beyond this wavelength, the signal became too weak and was not distinguishable from the background noise. The photocurrent for λ < 1.7 μm was in good agreement with the absorbance spectrum of the BHJ film (Figure S3A) and originated from photonic charge generation. Incident photons with energies larger than the effective bandgap gave rise to inter-band transitions of electrons, as depicted in Figure 1E, which increased the free carrier density in the device. The excess carriers raised the photocurrent and induced a V_{oc} in Figure 1B. While the photocurrent at reverse bias was obvious, the large background current injected at forward bias obscured the photoresponse under positive voltage in Figure 1B. However, the numbers of photogenerated carriers were similar under forward and reverse biases, as measured by lock-in homodyne detection. Thus, the responsivity under the photonic mechanism was nearly identical for ±0.2 V, as shown in Figure 1D.

Beyond the photonic limit (λ < 1.7 μm for CDT-TQ:$PC_{71}BM$ due to a charge-transfer bandgap[29] of ∼0.8 eV), the detector responded to MWIR/LWIR radiation through bolometric effects. The range of device responsivity was 3 mA/W to 0.05 A/W for λ between 3 and 8 μm in Figure 1D, in which the light source was a blackbody adjusted to radiate at different peaks λ. The absorption of photons with energies smaller than the BHJ effective bandgap led to temperature changes in the materials. The current−voltage characteristic under MWIR/LWIR radiation in Figure 1C did not feature a V_{oc}, because the response was mainly thermal modulation of resistivity and did not correspond to a large excess of accumulated carriers to induce V_{oc}. In Figure 1C,D, the magnitude of the bolometric current was larger at forward bias than at reverse bias; the resulting responsivity was higher at 0.2 V than −0.2 V and different from the photonic regime. Furthermore, a slight increase in responsivity with longer-wavelength MWIR/LWIR light was influenced by the presence of a glass substrate, as presented in Figure S3B and in Experimental Section, showing the transmittance spectra estimated from Fourier transform infrared (FTIR) spectroscopy. The glass substrate showed increasing absorbance for λ from 5 to 16 μm and heated up more at longer wavelengths, consequently leading to a larger change in BHJ resistivity.

The boundary between photonic and thermal operations corresponds to the charge-transfer bandgap of the semiconducting materials. The photonic mechanism was applicable for the spectral range where the photon energy was higher than the BHJ effective bandgap. Meanwhile, in response to radiation

https://doi.org/10.1021/acsami.2c17477
ACS Appl. Mater. Interfaces XXXX, XXX, XXX−XXX

in the low energy range extending into the LWIR, organic detectors are operated by temperature-dependent bolometric mechanisms that include intra-band thermal activation and sub-bandgap transitions of charges, as illustrated in Figure 1F. Figure 1F is drawn to present two possible bolometric contributions in noncrystalline semiconductors such as a-Si and organic BHJs. The intra-band transition represents thermally activated hopping transport that dictates the charge mobility. The sub-bandgap transition depicts the charge trap-and-release process through sub-bandgap states[31,32] according to the Shockley–Read–Hall (SRH) model, which affects the mobile charge density.

Contributions to the Bolometric Current. The change in bolometric current is commonly attributed to the temperature-dependent mobility. However, the current I is proportional to both mobile charge density N_m and mobility μ by $I = qN_m\mu E$, where q is the electron charge and E is the electric field. The following measurements aimed to clarify the contributions to the bolometric response, especially to account for the change in N_m due to thermal generation through sub-bandgap trap states that has been mostly neglected in the organic bolometer literature. A recent study[33] showed mid-gap states to be a major noise source in organic photodiodes, which motivated us to examine the effect of sub-bandgap states in the context of the bolometric response.

In Figure 2A, the current–voltage (I–V) characteristics of a CDT-TQ:$PC_{71}BM$ photodiode displayed an increasing current with a higher device temperature. The change in current was purely a bolometric response because the device temperature T was set by a stage temperature controller in the dark with no possible photonic excitation. The current measured at 26–38 °C was normalized to the current at 22 °C, as shown in Figure 2B; the resulting ratio $I_T/I_{22°C}$ was higher under reverse bias than forward bias. This bias dependence of the $I_T/I_{22°C}$ ratio demanded a closer examination to explain why the device was more sensitive to temperature changes under reverse bias. To gain complementary information to I–V characteristics, we carried out capacitance–frequency spectroscopy[33−38] to measure the sub-bandgap DOS, subsequently delineate the changes in N_m and μ as a function of bias, and in turn clarify their roles in the bolometric response.

From capacitance–frequency measurements, the sub-bandgap DOS was extracted as a function of temperature in Figure 2C. The equation for DOS calculations is included in the Supplementary Experimental Section. The sub-bandgap DOS, or, namely, the trap density, increased by ∼30% as the temperature rose from 22 to 38 °C, and the edge of DOS shifted to occupy deeper energy levels in the bandgap. These temperature effects on trap DOS indicated that upon heating there were more charges involved in the trap-and-release process, with SRH transitions through sub-gap states contributing to thermal charge generation. The thermal generation rate is expressed by[33]

$$G = \frac{\beta_{SRH} N_t n_i}{2\cosh\left(\frac{E_t - E_i}{k_B T}\right)} \quad (1)$$

where β_{SRH} is the recombination rate, n_i is the intrinsic charge concentration, E_i is the mid-gap energy, and N_t is the trap DOS at energy E_t within the bandgap. We define sub-bandgap (or sub-gap) states to represent all the states within the bandgap of the semiconductor regardless of their energy level, while mid-gap states are located near the middle of the bandgap. Thus, mid-gap states are a subcategory of sub-gap states. Due to the cosh function, the highest generation rate is achieved around E_i, and then G decreases exponentially toward the valence and conduction band. We applied a simplifying assumption to eq 1 and calculated the change in G at mid-gap only by setting $E_t = E_i$. As such, the denominator in eq 1 is reduced to a constant, and the change in G with temperature is simplified to

$$G(T)/G_{22°C} = N_t(T)/N_{t,22°C} \quad (2)$$

where the generation rate normalized to 22 °C is mainly dependent on the change in trap density with temperature. The relation expressed in eq 2 was calculated by using the peak trap DOS at ∼0.33 eV, as measured in Figure 2C, and this trap energy level is near the middle of the effective bandgap for this BHJ.

Figure 2D shows the measured bolometric current ratio $I_T/I_{22°C}$ versus device temperature for the device under forward bias (red data) and reverse bias (blue data). The error bars at each temperature encompassed the data from 0.3 to 1 V for forward bias and −1 to −0.3 V for reverse bias. The thermal generation ratios $G_T/G_{22°C}$ were also calculated based on eq 2 and added as the black line, while the charge mobility ratios were plotted as the dashed line in Figure 2D. The mobility was determined by fitting I–V measurements to the space-charge-limited current model[40] in Figure S4, and the extracted mobility was normalized to the value at 22 °C to obtain the mobility ratio $\mu_T/\mu_{22°C}$.

In Figure 2D, $I_T/I_{22°C}$ under forward bias matched well to the change in mobility with temperature. However, for $I_T/I_{22°C}$ under reverse bias, its temperature dependence was higher than expected from the mobility change alone. The product of G and μ (gray dotted line) was required to account for the bolometric response under reverse bias. The difference in $I_T/I_{22°C}$ between forward and reverse biases was due to the magnitude of injected charges. Thermal generation occurred under both bias polarities, but its manifestation was buried under forward bias because of the high concentration of injected charge ($N_m \gg qG$). Meanwhile, under reverse bias, the background current level was comparable to thermally generated charges ($N_m \sim qG$), making it easier to see the thermal generation contribution. This comparison is by ratio and not the absolute value of bolometric current.

In addition, it was inferred from Figure 2D that shallower traps would contribute more to the thermal sensitivity of the detector. Between the mobility dependent on shallow traps and the thermal generation factor through deep mid-gap states, the mobility was more sensitive to temperature change than thermal generation, as seen in the faster rise of the dashed line than the solid line in Figure 2D. The shallow traps at the bandtail facilitated the thermal response, as illustrated in Figure 1F. With abundant states at the bandtail, the thermally activated electrons were easily promoted to the conduction band and increased the hopping mobility, as associated with the activation energy of the carriers.

Figure 2E illustrates the two contributing factors to bolometric current as evident in the data: one being the hopping transport that dictates temperature-dependent mobility and the other one being sub-bandgap states that promote charge concentration with increasing device temperature. For the former, the inset illustrates the energetic barriers faced by the charges when traveling through disordered materials. The defects and boundaries between crystalline and amorphous regions in disordered materials may act as barriers that hinder

https://doi.org/10.1021/acsami.2c17477
ACS Appl. Mater. Interfaces XXXX, XXX, XXX−XXX

charge transport. The energetic barrier is usually correlated to the activation energy E_a. Hopping transport is thermally activated, and hence, the inset shows that at higher temperatures, the hopping transport can be more efficient with sufficient energy to overcome the energetic barriers. The green arrow in the inset indicates successful hopping transport, while the brown blocked arrow indicates a charge without sufficient energy to hop over the energetic barrier.

Correlation of TCR to Parameters of Activation Energy, Sub-Bandgap DOS, and Effective Bandgap. Having clarified the roles of intra-band and sub-bandgap transitions in the organic MWIR/LWIR response, next, we examined the series of BHJs in Figure 3 to correlate their TCRs to electronic properties at the mobility edge and sub-bandgap trap states. Despite the diversity of organic semiconductors, prior work on organic MWIR/LWIR detectors has mostly utilized poly(3,4-ethylenedioxythiophene) polystyrene sulfonate PEDOT:PSS composites[41−44] as the active material.

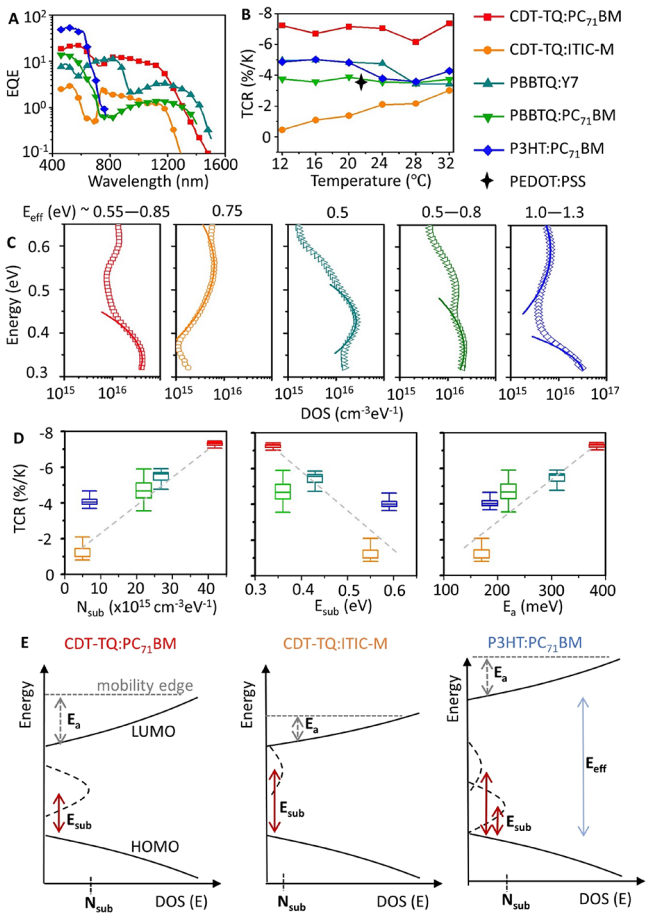

Figure 3. Correlation of TCR to sub-bandgap characteristics of various organic BHJ photodiodes. (A) External quantum efficiency versus wavelengths in the photovoltaic regime, with the devices biased at −0.1 V. (B) TCR versus temperature, the devices biased at 0.1 V. The PEDOT:PSS value is taken from ref 13. (C) DOS versus energy with respect to the band edge. The solid lines are fits based on Gaussian distributions. (D) TCR versus (left) the peak values of sub-bandgap trap DOS, (middle) their corresponding trap energy levels, and (right) the activation energies for charge carriers to reach the mobility edge. The TCR box-and-whisker markers indicate the range of values measured under applied biases of ±0.1 V. (E) Illustrations on how the parameters of trap density N_{sub}, trap energy level E_{sub}, and carrier activation energy E_a vary between three examples of BHJs. Increasing N_{sub} and E_a raises TCR, and small E_{sub} promotes SRH transitions correlated to high TCR.

Here, we showed that expanding beyond this standard material increases TCR and broadens the device spectral range to encompass both the visible to SWIR (Figure 3A) and MWIR/LWIR regions (Figure 3B), whereas PEDOT:PSS is not a strong absorber in the vis−NIR.

More importantly, through the BHJ series, we pinpoint the characteristics essential to tune the TCR. For instance, when pairing the same SWIR polymer CDT-TQ with either a fullerene or a non-fullerene acceptor, the TCR differed by up to 7-fold, as shown in Figure 3B. The origin of this significant change is revealed for the first time in the following analysis to explain how the sub-bandgap trap DOS, mobility activation energy, and effective bandgap are key design parameters for controlling the device TCR.

The definition of TCR[13,41] is

$$\mathrm{TCR} = \frac{R_2 - R_1}{(T_2 - T_1)R_1} = \frac{dR}{dT}\frac{1}{R} \quad (3)$$

where R_1 and R_2 represent the resistance of the device measured at T_1 and T_2, respectively. Typically, the sign of TCR is negative in semiconducting materials and positive in metallic materials,[12,17] and a high TCR is a prerequisite for an efficient bolometer. The TCR values of Figure 3B were extracted from the $I-V$ characteristics as a function of temperature, as found in Figure S5. We have also tested devices using single polymers and not BHJs, but the thermal response is weak compared to BHJs (Figure S5).

Among the devices in Figure 3B, the one with CDT-TQ:$PC_{71}BM$ exhibited the highest TCR of −7%/K, and this value surpasses the performance of a-Si,[1,25] V_2O_5,[1,25] and carbon nanotubes[17] and is comparable to graphene.[45] Meanwhile, the same donor polymer with a different non-fullerene acceptor CDT-TQ:ITIC-M showed the lowest TCR of <−2%/K. This interesting result from changing acceptors suggested a relation to energetic disorder[29] and motivated us to examine the sub-bandgap DOS for clues that explain the TCR trend.

Here, we explain the process to extract four parameters that describe the properties of BHJ: trap DOS magnitude N_{sub} and its corresponding energy E_{sub}, mobility activation energy E_a, and effective bandgap E_{eff}. Based on the capacitance−frequency measurements in Figure S6A, the sub-bandgap DOS was extracted for each BHJ in Figure 3C and Figure S6B. Since sub-bandgap trap states are commonly described by Gaussian distributions, the peak in the DOS was fit to a Gaussian function indicated by the solid line, and the fit values are listed in Table S1. The DOS magnitude (x-axis in Figure 3C), namely, the sub-bandgap trap concentration at the Gaussian peak, is denoted by N_{sub}, and the energy (y-axis in Figure 3C) of peak trap concentration is denoted by E_{sub}. The effective bandgap E_{eff}[46] is defined by the difference between the donor's highest occupied molecular orbital (HOMO) and the acceptor's lowest unoccupied molecular orbital (LUMO) (Figure S6C). The estimated E_{eff} for each BHJ is listed in Figure 3C. Furthermore, from the $I-V$ characteristics fitted to the SCLC model, the charge mobility as a function of temperature was obtained, from which the Arrhenius activation energy E_a was determined for each BHJ, as shown in Figure S7.

In Figure 3D, the relations of TCR to the extracted N_{sub}, E_{sub}, and E_a values are presented to pinpoint physical

https://doi.org/10.1021/acsami.2c17477
ACS Appl. Mater. Interfaces XXXX, XXX, XXX−XXX

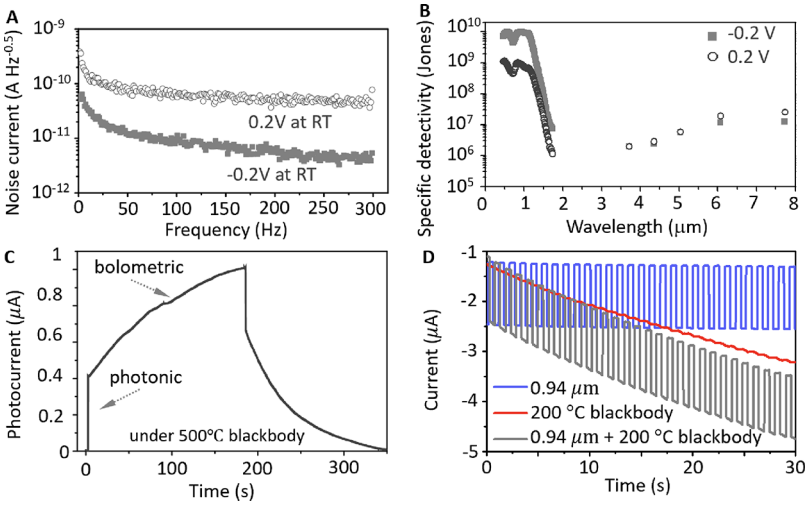

Figure 4. Signal-to-noise characteristics and response speed of a detector with CDT-TQ:$PC_{71}BM$. (A) Noise current versus frequency, with different biases on the device measured at room temperature ~24 °C. (B) Specific detectivity versus incident wavelength. (C) Photocurrent versus time, with the device biased at −0.2 V and exposed to constant radiation from a 500 °C blackbody. (D) Device current at −0.2 V versus time, where the light sources [0.94 μm (blue, 0.2 mW/cm^2), 200 °C blackbody (red, 13 mW/cm^2), or together (black)] were modulated at 1 Hz through an optical chopper. The peak wavelength for a 200 °C blackbody is ~6 μm.

characteristics that impact the bolometric sensitivity of BHJs. Generally, a larger concentration N_{sub} of sub-bandgap traps correlated to higher TCR, since more available trap states would facilitate SRH transitions that generate charges by thermal activation and increase the bolometric response. On the other hand, when the energy at peak trap concentration E_{sub} was farther away from HOMO (higher E_{sub} values), the device TCR decreased. With regard to the mobility activation energy, higher E_a increased TCR. For hopping transport in organic BHJs, a large activation energy meant that states at band edges were far from the mobility edge. As such, if the band-edge states were broadly distributed over different energy levels, a temperature change would result in a large change in conductivity and hence high TCR.

The combinations of donor PBBTQ with different acceptors showed TCR in between the two extremes of CDT-TQ combinations. The PBBTQ and CDT-TQ polymers are SWIR-bandgap materials with a photonic response beyond 1 μm. For contrast, we also examined a visible bandgap BHJ using P3HT. Here, we pick three representative cases for comparison, as presented in Figure 3E. E_{sub} was near the middle of the effective bandgap E_{eff} in CDT-TQ:$PC_{71}BM$ with the highest TCR. For the other two devices, E_{sub} shifted to band edges. This shift in the DOS would lead to reduced thermally activated charges through mid-gap states upon thermal activation, which is described by eq 1, where the thermal generation rate was maximum at mid-gap.

Meanwhile, because of the reduced disorder from the non-fullerene acceptor ITIC-M as evident in the DOS, the E_a and N_{sub} of CDT-TQ:ITIC-M were smaller. These characteristics, along with a larger difference in energy from the HOMO edge to the peak trap energy E_{sub}, led to as much as a 7-fold decrease in TCR for CDT-TQ:ITIC-M when compared to CDT-TQ:$PC_{71}BM$. For the P3HT:$PC_{71}BM$ device, the TCR is higher than expected, considering the relatively small N_{sub} and large E_{sub} for the mid-gap states near 0.6 eV. We attribute higher-than-expected TCR to DOS states near the band edge (near 0.3 eV as fitted in Figure 3E), which contributed to thermally activated transitions. The additional consideration for the P3HT:$PC_{71}BM$ combination was that its effective bandgap was much higher than narrow-bandgap BHJs, resulting in larger resistance that reduced TCR according to eq 3. This E_{eff} influence was also a reason why prior PEDOT:PSS (bandgap ~1.7 eV) bolometers did not show as high TCR as the materials in this report.

With the insights gained from analyzing the BHJ series, we now have a handle on how to choose materials and adjust the electronic DOS to enhance/suppress bolometric current. MWIR/LWIR response will be increased in materials with a reduced effective bandgap. If broadband SWIR to LWIR response is desired, thermal SRH generation may be enhanced by modifying sub-bandgap states through dopants, particularly at an energy level near the middle of the bandgap. However, this approach might present a trade-off between SWIR dark current and LWIR response. Alternatively, if only SWIR spectral bands are desired, the bolometric current can be suppressed by reducing trap DOS and adopting materials with a sharp rise in DOS at band edges.

It should be noted that there is a large parameter space and numerous processing variables that would affect bolometric effects, and that is why we down-selected and focused this study on BHJ compositions that provided the highest photonic response. From these compositions, the BHJ blends were deposited to be within 150−180 nm; thus, the devices were comparable in active film thicknesses. From this group of optimized photonic devices, we were able to extract basic physical parameters such as sub-gap DOS and mobility to infer design rules governing the bolometric response, as discussed in this work. Methods to adjust the sub-gap DOS in a semiconducting organic material include adjusting donor-to-acceptor ratios in the BHJ, adding dopants, annealing, and so on. In the future, it will be interesting to extend the study to other material systems as well, such as organic/inorganic hybrid active layer systems, to consider different choices in selecting an appropriate sub-gap DOS distribution for thermal signal detection.

Specific Detectivity and Response Speed. The metric of specific detectivity D^* indicates the signal-to-noise ratio or

https://doi.org/10.1021/acsami.2c17477
ACS Appl. Mater. Interfaces XXXX, XXX, XXX−XXX

the detection limit and is defined as $D^* = R A^{0.5}/S_n$, where R is the responsivity, A is the active area of the detector, and S_n is the noise spectral density. In Figure 4A, the CDT-TQ:$PC_{71}BM$ detector showed higher noise at forward bias because of the large injection current. The detector D^* was calculated based on the responsivity (Figure 1D) and noise (Figure 4A) measurements and is presented in Figure 4B. In the SWIR region, the D^* reached up to 10^{10} Jones and was higher at reverse bias due to lower noise than at forward bias. In the MWIR/LWIR region, the specific detectivity was 10^7 Jones and similar for both bias polarities, since the higher responsivity at forward bias was offset by a higher noise level, resulting in the same D^* compared to the values at reverse bias.

Regarding the detector speed in the two spectral regions, Figure 4C shows a dramatic difference in response time under photonic versus bolometric mechanisms. The transient photocurrent in Figure 4C was taken under a blackbody at a temperature of 500 °C. Since this light source emitted over a broad spectrum across the SWIR and MWIR/LWIR (1.1 to 15 μm, as calculated in Figure S2), the detector photocurrent was a combination of photonic and thermal responses. There was a clear fast photonic response in which photogeneration of electron−hole pairs enabled rapid current changes, followed by a much slower change in the device to establish thermal equilibrium between the sensor element and its surroundings. Figure 4D displays another result under an incident light that was modulated at 1 Hz and from a combination of 940 nm LED and 200 °C blackbody with a peak wavelength of 6.1 μm. The signal that followed the 1 Hz modulation was from a photonic contribution in response to 940 nm light, while the slow drift was due to the heat from the blackbody. Hence, the photonic and thermal response can be decoupled and distinguished by the sampling speed. On this note, we have seen that some reports for MWIR/LWIR devices presented detector bandwidths based on values measured under NIR/SWIR photonic light sources. This approach would cause an overestimation of the detector bandwidth, because the fast photonic response was mistaken for the MWIR/LWIR response frequency. We caution that bandwidth measurements should be carried out with a light source that matches the reported spectral range.

The time constant for a bolometric response is typically in the range of tens of milliseconds.[17,22] When we exposed the photodiode with CDT-TQ:$PC_{71}BM$ to a 2.25 μm laser that was modulated at ∼4 Hz, the bolometric current in Figure S8 was able to respond at this frequency under a low laser power of 0.2 $\mu W/cm^2$, which allowed fast establishment of thermal equilibrium. However, the study here did not optimize the device geometry to push for faster response and higher D^*, because our focus was to understand the effects of material properties (E_a, N_{sub}, and E_{eff}) on current generation mechanisms. In the future, device optimization techniques, such as suspending the active film in vacuum,[17] integrating a plasmonic metasurface,[22] and reducing the thermal capacity and incorporating resonant modes in the detector,[47] can be used to increase device metrics including detectivity and response speed.

CONCLUSIONS

Our detectors based on narrow-bandgap BHJs have combined photonic and bolometric mechanisms to achieve broadband detection spanning the visible to LWIR, with photonic charge generation for visible to SWIR light and bolometric effects for the MWIR to LWIR. This study identified the key material parameters (mobility activation energy E_a, density of trap states N_{sub}, and effective bandgap E_{eff}) for controlling the TCR in organic detectors and revealed the important role of sub-bandgap states in the bolometric response of BHJs. The findings guide future material choices, such that increasing N_{sub} and E_a raises TCR, and a small E_{eff} promotes SRH transitions correlated to high TCR.

The abundance of sub-bandgap states in organic narrow-bandgap systems led to a high TCR that exceeds typical values of conventional a-Si or V_2O_5 bolometer materials. With the knowledge gained here to modify material and device configurations, future optimization in detectivity and response speed in organic IR detectors is promising, to offer a technology with ease of fabrication and high performance without cooling systems.

EXPERIMENTAL SECTION

Materials. The polymer CDT-TQ was synthesized according to ref 35. The polymer PBBTQ was synthesized as described in ref 30. All the other materials are purchased and used without any treatment. The compositions of BHJ films are summarized in Table 1.

Device Fabrication. The glass or polyethylene naphthalate (PEN) substrates with patterned indium tin oxide (ITO) electrodes (∼15 Ω/sq) were cleaned in detergent, deionized water, acetone, and IPA sequentially and each for 10 min. The n-type charge collection layer ZnO was deposited by spin-coating the ZnO nanoparticles, resulting in a thin film of ∼10 nm. The active BHJ layers were prepared by spin-coating in a nitrogen-filled glovebox. The samples were then transferred to a vacuum chamber to deposit the p-type MoO_3 layer and Ag electrode. The active area was defined by the overlap between the ITO electrode and the top Ag electrode. All the devices are encapsulated and placed under white light for 5 min to passivate trap states.

Device Characterization. All the devices were characterized in the ambient atmosphere. The photonic response versus wavelength was measured under monochromatic light. The illumination was modulated at 314 Hz by an optical chopper. The photocurrent from the device was amplified through a preamplifier (SRS 570) and then measured by a lock-in amplifier (SRS 510). The monochromatic light intensity was calibrated by a Ge detector (Newport 818IR/DB). The response to MWIR/LWIR signals was measured by exposing the detector to a blackbody operated at different temperatures. The intensity of MWIR/LWIR radiation was calibrated by a mercury-cadmium-telluride detector (Thorlabs, PDAVJ10). The $I-V$ characteristics were measured by an electrometer (Keithley 2400). The capacitance−frequency data were measured by a potentiostat (BioLogic SP-200). The noise current was captured by a spectrum analyzer (HP 89410A).

In Figure 2, the device temperature was kept constant by a stage temperature controller, which maintained a steady state in the device more easily than by using a blackbody radiator. In Figure 4, the specific detectivity was calculated at ∼310 Hz for the SWIR region and 5.6 mHz for the MWIR/LWIR region.

The FTIR spectra measured for the glass substrate with and without the BHJ layer are shown in Figure S3B. The glass substrate exhibited broad absorption across MWIR/LWIR, while the absorption by the BHJ was indicated by specific peaks due to resonant absorption of various functional groups. The BHJ absorbance was much lower than the thick glass substrate. Thus, the glass absorbed most of the radiation and raised the temperature of the device, which then induced a resistance change in the semiconducting BHJ. The bolometric responsivity increased from 3.5 to 8 μm in Figure 1D because of increasing absorption by the glass substrate.

The heat capacity of the CDT-TQ:$PC_{71}BM$ BHJ was estimated from differential scanning calorimetry (DSC). The heat capacity of

https://doi.org/10.1021/acsami.2c17477
ACS Appl. Mater. Interfaces XXXX, XXX, XXX−XXX

the CDT-TQ:$PC_{71}BM$ BHJ was about 2.8 to 3.1 Jg^{-1} K^{-1} as presented in Figure S3C for the temperature range from 0 to 60 °C, which is larger than that of the glass substrate, which is around 0.84 Jg^{-1} K^{-1}. Thus, the temperature increase under the same intensity radiation would be higher in glass than in the BHJ materials. Since the glass substrate showed higher IR absorption and lower heat capacity than BHJ, the thermal response in our organic bolometers was influenced by the underlying substrate. However, the influence is mainly on the response speed (slower speed with a large substrate), and the TCR value at equilibrium is dependent only on the BHJ materials and not on the substrate.

For our detectors on 1.1 mm thick glass substrates, the large heat capacity of the glass hindered the response speed. By switching to a thin 0.125 mm plastic PEN substrate, the rise/fall time of the device was reduced to ∼20 s in Figure S8, which was faster than the device on glass substrates with a rise/fall time of ∼150 s.

■ ASSOCIATED CONTENT

Supporting Information

The Supporting Information is available free of charge at https://pubs.acs.org/doi/10.1021/acsami.2c17477.

Equations for device characterization and fitting, parameters for the Gaussian function to fit the DOS, and additional figures (molecular structures, spectra for blackbody radiation, absorption and FTIR spectra, space-charge-limited current, current vs temperature, capacitance vs frequency, and temperature-dependent mobility) (PDF)

■ AUTHOR INFORMATION

Corresponding Author

Tse Nga Ng − *Department of Electrical and Computer Engineering, University of California San Diego, La Jolla, California 92093-0407, United States;* orcid.org/0000-0001-6967-559X; Email: tnn046@ucsd.edu

Authors

Ning Li − *Department of Electrical and Computer Engineering, University of California San Diego, La Jolla, California 92093-0407, United States; School of Electronic and Optical Engineering, Nanjing University of Science and Technology, Nanjing, CN 210094, People's Republic of China;* orcid.org/0000-0003-3382-341X

Insun Park − *Samsung Advanced Institute of Technology, Samsung Electronics, Co., Ltd., Suwon-si, Gyeonggi-do 16678, South Korea*

Jarrett H. Vella − *Sensors Directorate, Air Force Research Laboratory, Wright−Patterson Air Force Base, Dayton 45433-7131 Ohio, United States*

Soong Ju Oh − *Department of Materials Science and Engineering, Korea University, Seoul 02841, Republic of Korea;* orcid.org/0000-0003-1434-8844

Jason D. Azoulay − *School of Polymer Science and Engineering, The University of Southern Mississippi, Hattiesburg, Mississippi 39406, United States;* orcid.org/0000-0003-0138-5961

Dong-Seok Leem − *Samsung Advanced Institute of Technology, Samsung Electronics, Co., Ltd., Suwon-si, Gyeonggi-do 16678, South Korea*

Complete contact information is available at: https://pubs.acs.org/10.1021/acsami.2c17477

Author Contributions

N.L. and T.N.N. conceived the idea and designed the experiments. I.P. and D.-S.L. provided the PBBTQ polymer and contributed to refining hypotheses. J.H.V. and S.J.O. contributed to the hypotheses and experimental plans. J.D.A provided the CDT-TQ polymer. The first draft of the manuscript was written by N.L. All the authors contributed to the editing of the manuscript.

Notes

The authors declare no competing financial interest.

■ ACKNOWLEDGMENTS

The authors N.L. and T.N.N. acknowledge the support from Samsung Advanced Institute of Technology. J.D.A. acknowledges the support from the National Science Foundation (OIA-1757220) and Air Force Office of Scientific Research (AFOSR) Organic Materials Chemistry Program (Grant FA9550-20-1-0353, Program Manager: Dr. Kenneth Caster). We acknowledge Gaoweiang Dong and Prof. Shengqiang Cai from the Department of Mechanical and Aerospace Engineering at the University of California San Diego for their assistance on differential scanning calorimetry measurements.

■ REFERENCES

(1) Rogalski, A.*Infrared and Terahertz Detectors*; CRC Press; 2019; pp. 11−14.

(2) García De Arquer, F. P.; Armin, A.; Meredith, P.; Sargent, E. H. Solution-Processed Semiconductors for next-Generation Photodetectors. *Nat. Rev. Mater.* **2017**, *2*, 16100.

(3) Li, N.; Mahalingavelar, P.; Vella, J. H.; Leem, D.-S.; Azoulay, J. D.; Ng, T. N. Solution-Processable Infrared Photodetectors: Materials, Device Physics, and Applications. *Mater. Sci. Eng., R* **2021**, *146*, No. 100643.

(4) Wang, C.; Zhang, X.; Hu, W. Organic Photodiodes and Phototransistors toward Infrared Detection: Materials, Devices, and Applications. *Chem. Soc. Rev.* **2020**, *49*, 653−670.

(5) Lee, S. H.; Yusoff, A. R. b. M.; Lee, C.; Yoon, S. C.; Noh, Y.-Y. Toward Color-Selective Printed Organic Photodetectors for High-Resolution Image Sensors: From Fundamentals to Potential Commercialization. *Mater. Sci. Eng., R* **2022**, *147*, No. 100660.

(6) Wadsworth, A.; Hamid, Z.; Kosco, J.; Gasparini, N.; McCulloch, I. The Bulk Heterojunction in Organic Photovoltaic, Photodetector, and Photocatalytic Applications. *Adv. Mater.* **2020**, *32*, 2001763.

(7) Lan, Z.; Zhu, F. Electrically Switchable Color-Selective Organic Photodetectors for Full-Color Imaging. *ACS Nano* **2021**, *15*, 13674.

(8) Li, N.; Eedugurala, N.; Leem, D. S.; Azoulay, J. D.; Ng, T. N. Organic Upconversion Imager with Dual Electronic and Optical Readouts for Shortwave Infrared Light Detection. *Adv. Funct. Mater.* **2021**, *31*, 2100565.

(9) Kim, H.; Wu, Z.; Eedugurala, N.; Azoulay, J. D.; Ng, T. N. Solution-Processed Phototransistors Combining Organic Absorber and Charge Transporting Oxide for Visible to Infrared Light Detection. *ACS Appl. Mater. Interfaces* **2019**, *11*, 36880−36885.

(10) Shin, C.; Li, N.; Seo, B.; Eedugurala, N.; Azoulay, J. D.; Ng, T. N. Heterojunction Bilayers Serving as a Charge Transporting Interlayer Reduce the Dark Current and Enhance Photomultiplication in Organic Shortwave Infrared Photodetectors. *Mater. Horiz.* **2022**, *9*, 2172−2179.

(11) Vella, J. H.; Huang, L.; Eedugurala, N.; Mayer, K. S.; Ng, T. N.; Azoulay, J. D. Broadband Infrared Photodetection Using a Narrow Bandgap Conjugated Polymer. *Sci. Adv.* **2021**, *24*, No. eabg2418.

(12) Pfattner, R.; Lebedev, V.; Laukhina, E.; Kumar, S. C.; Esteban-Martin, A.; Ramaiah-Badarla, V.; Ebrahim-Zadeh, M.; de Arquer, F. P. G.; Konstantatos, G.; Laukhin, V.; Rovira, C.; Veciana, J. A Highly Sensitive Pyroresistive All-Organic Infrared Bolometer. *Adv. Electron. Mater.* **2015**, *1*, 1500090.

(13) Håkansson, A.; Shahi, M.; Brill, J. W.; Fabiano, S.; Crispin, X. Conducting-Polymer Bolometers for Low-Cost IR-Detection Systems. *Adv. Electron. Mater.* **2019**, *5*, 1800975.
(14) Jiang, W.; Zheng, T.; Wu, B.; Jiao, H.; Wang, X.; Chen, Y.; Zhang, X.; Peng, M.; Wang, H.; Lin, T.; Shen, H.; Ge, J.; Hu, W.; Xu, X.; Meng, X.; Chu, J.; Wang, J. A Versatile Photodetector Assisted by Photovoltaic and Bolometric Effects. *Light: Sci. Appl.* **2020**, *9*, 160.
(15) Lhuillier, E.; Scarafagio, M.; Hease, P.; Nadal, B.; Aubin, H.; Xu, X. Z.; Lequeux, N.; Patriarche, G.; Ithurria, S.; Dubertret, B. Infrared Photodetection Based on Colloidal Quantum-Dot Films with High Mobility and Optical Absorption up to THz. *Nano Lett.* **2016**, *16*, 1282−1286.
(16) Rogalski, A.; Kopytko, M.; Martyniuk, P. 2D Material Infrared and Terahertz Detectors: Status and Outlook. *Opto-Electron. Rev.* **2020**, *28*, 107−154.
(17) Itkis, M. E.; Borondics, F.; Yu, A.; Haddon, R. C. Bolometric Infrared Photoresponse of Suspended Single-Walled Carbon Nanotube Films. *Science* **2006**, *312*, 413−416.
(18) Trudeau, C.; Beaupré, P.; Bolduc, M.; Cloutier, S. G. All Inkjet-Printed Perovskite-Based Bolometers. *npj Flexible Electron.* **2020**, *4*, 34.
(19) Zhang, F.; Zang, Y.; Huang, D.; Di, C. A.; Zhu, D. Flexible and Self-Powered Temperature-Pressure Dual-Parameter Sensors Using Microstructure-Frame-Supported Organic Thermoelectric Materials. *Nat. Commun.* **2015**, *6*, 8356.
(20) Joo, Y.; Huang, L.; Eedugurala, N.; London, A. E.; Kumar, A.; Wong, B. M.; Boudouris, B. W.; Azoulay, J. D. Thermoelectric Performance of an Open-Shell Donor-Acceptor Conjugated Polymer Doped with a Radical-Containing Small Molecule. *Macromolecules* **2018**, *51*, 3886−3894.
(21) Beretta, D.; Neophytou, N.; Hodges, J. M.; Kanatzidis, M. G.; Narducci, D.; Martin-Gonzalez, M.; Beekman, M.; Balke, B.; Cerretti, G.; Tremel, W.; Zevalkink, A.; Hofmann, A. I.; Müller, C.; Dörling, B.; Campoy-Quiles, M.; Caironi, M. Thermoelectrics: From History, a Window to the Future. *Mater. Sci. Eng., R* **2019**, *138*, 100501.
(22) Stewart, J. W.; Vella, J. H.; Li, W.; Fan, S.; Mikkelsen, M. H. Ultrafast Pyroelectric Photodetection with On-Chip Spectral Filters. *Nat. Mater.* **2020**, *19*, 158−162.
(23) Street, R. A.*Hydrogenated Amorphous Silicon*; Cambridge University Press, 1991; pp. 255−275.
(24) Li, J.; Yuan, N. Temperature Sensitivity of Resistance of VO 2 Polycrystalline Films Formed by Modified Ion Beam Enhanced Deposition. *Appl. Surf. Sci.* **2004**, *233*, 252−257.
(25) Henini, M.; Razeghi, M.*Handbook of Infra-red Detection Technologies*; Elsevier, 2002; pp. 1−518.
(26) Arora, H.; Dong, R.; Venanzi, T.; Zscharschuch, J.; Schneider, H.; Helm, M.; Feng, X.; Cánovas, E.; Erbe, A. Demonstration of a Broadband Photodetector Based on a Two-Dimensional Metal−Organic Framework. *Adv. Mater.* **2020**, *32*, 1907063.
(27) Wang, S.; Li, Q. Design, Synthesis and Processing of PVDF-Based Dielectric Polymers. *IET Nanodielectr.* **2018**, *1*, 80−91.
(28) Aleksandrova, M.; Jagtap, C.; Kadam, V.; Jadkar, S.; Kolev, G.; Denishev, K.; Pathan, H. M. An Overview of Microelectronic Infrared Pyroelectric Detector. *Eng. Sci.* **2021**, *16*, 82−89.
(29) Wu, Z.; Li, N.; Eedugurala, N.; Azoulay, J. D.; Leem, D.-S.; Ng, T. N. Noise and Detectivity Limits in Organic Shortwave Infrared Photodiodes with Low Disorder. *npj Flexible Electron.* **2020**, *4*, 6.
(30) Park, I.; Kim, C.; Kim, R.; Li, N.; Lee, J.; Kwon, O. K.; Choi, B.; Ng, T. N.; Leem, D.-S. High Performance Shortwave Infrared Organic Photodetectors Adopting Thiadiazole Quinoxaline-Based Copolymers. *Adv. Opt. Mater.* **2022**, *10*, 2200747.
(31) Hawks, S. A.; Li, G.; Yang, Y.; Street, R. A. Band Tail Recombination in Polymer: Fullerene Organic Solar Cells. *J. Appl. Phys.* **2014**, *116*, No. 074503.
(32) Zhou, J.; Raihan Miah, M. A.; Yu, Y.; Zhang, A. C.; Zeng, Z.; Damle, S.; Niaz, I. A.; Zhang, Y.; Lo, Y.-H. Room-Temperature Long-Wave Infrared Detector with Thin Double Layers of Amorphous Germanium and Amorphous Silicon. *Opt. Express* **2019**, *27*, 37056.
(33) Kublitski, J.; Hofacker, A.; Boroujeni, B. K.; Benduhn, J.; Nikolis, V. C.; Kaiser, C.; Spoltore, D.; Kleemann, H.; Fischer, A.; Ellinger, F.; Vandewal, K.; Leo, K. Reverse Dark Current in Organic Photodetectors and the Major Role of Traps as Source of Noise. *Nat. Commun.* **2021**, *12*, 551.
(34) Street, R. A.; Yang, Y.; Thompson, B. C.; McCulloch, I. Capacitance Spectroscopy of Light Induced Trap States in Organic Solar Cells. *J. Phys. Chem. C* **2016**, *120*, 22169−22178.
(35) Wu, Z.; Zhai, Y.; Yao, W.; Eedugurala, N.; Zhang, S.; Huang, L.; Gu, X.; Azoulay, J. D.; Ng, T. N. The Role of Dielectric Screening in Organic Shortwave Infrared Photodiodes for Spectroscopic Image Sensing. *Adv. Funct. Mater.* **2018**, *28*, 1805738.
(36) Walter, T.; Herberholz, R.; Müller, C.; Schock, H. W. Determination of Defect Distributions from Admittance Measurements and Application to Cu(In,Ga)Se_2 Based Heterojunctions. *J. Appl. Phys.* **1996**, *80*, 4411−4420.
(37) Wang, S.; Kaienburg, P.; Klingebiel, B.; Schillings, D.; Kirchartz, T. Understanding Thermal Admittance Spectroscopy in Low-Mobility Semiconductors. *J. Phys. Chem. C* **2018**, *122*, 9795−9803.
(38) Xu, L.; Wang, J.; Hsu, J. W. P. Transport Effects on Capacitance-Frequency Analysis for Defect Characterization in Organic Photovoltaic Devices. *Phys. Rev. Appl.* **2016**, *6*, No. 064020.
(39) Vandewal, K.; Albrecht, S.; Hoke, E. T.; Graham, K. R.; Widmer, J.; Douglas, J. D.; Schubert, M.; Mateker, W. R.; Bloking, J. T.; Burkhard, G. F.; Sellinger, A.; Fréchet, J. M. J.; Amassian, A.; Riede, M. K.; McGehee, M. D.; Neher, D.; Salleo, A. Efficient Charge Generation by Relaxed Charge-Transfer States at Organic Interfaces. *Nat. Mater.* **2014**, *13*, 63−68.
(40) Murgatroyd, P. N. Theory of Space-Charge-Limited Current Enhanced by Frenkel Effect. *J. Phys. D: Appl. Phys.* **1970**, *3*, 151−156.
(41) Li, J.; Li, Z.; Wang, J.; Chen, X. Study of Conductive Polymer PEDOT: PSS for Infrared Thermal Detection. *Opt. Mater. Express* **2019**, *9*, 4474.
(42) Bubnova, O.; Khan, Z. U.; Wang, H.; Braun, S.; Evans, D. R.; Fabretto, M.; Hojati-Talemi, P.; Dagnelund, D.; Arlin, J. B.; Geerts, Y. H.; Desbief, S.; Breiby, D. W.; Andreasen, J. W.; Lazzaroni, R.; Chen, W. M.; Zozoulenko, I.; Fahlman, M.; Murphy, P. J.; Berggren, M.; Crispin, X. Semi-Metallic Polymers. *Nat. Mater.* **2014**, *13*, 190−194.
(43) Zhang, M.; Yeow, J. T. W. A Flexible, Scalable, and Self-Powered Mid-Infrared Detector Based on Transparent PEDOT: PSS/Graphene Composite. *Carbon* **2020**, *156*, 339−345.
(44) Li, Y.; Zhang, Y.; Li, T.; Tang, X.; Li, M.; Chen, Z.; Li, Q.; Sheng, Q.; Shi, W.; Yao, J. A Fast Response, Self-Powered and Room Temperature near Infrared-Terahertz Photodetector Based on a MAPbI3/PEDOT:PSS Composite. *J. Mater. Chem. C* **2020**, *8*, 12148−12154.
(45) Sassi, U.; Parret, R.; Nanot, S.; Bruna, M.; Borini, S.; De Fazio, D.; Zhao, Z.; Lidorikis, E.; Koppens, F. H. L.; Ferrari, A. C.; Colli, A. Graphene-Based Mid-Infrared Room-Temperature Pyroelectric Bolometers with Ultrahigh Temperature Coefficient of Resistance. *Nat. Commun.* **2017**, *8*, 14311.
(46) Eisner, F.; Foot, G.; Yan, J.; Azzouzi, M.; Georgiadou, D. G.; Sit, W. Y.; Firdaus, Y.; Zhang, G.; Lin, Y. H.; Yip, H. L.; Anthopoulos, T. D.; Nelson, J. Emissive Charge-Transfer States at Hybrid Inorganic/Organic Heterojunctions Enable Low Non-Radiative Recombination and High-Performance Photodetectors. *Adv. Mater.* **2022**, 2104654.
(47) Blaikie, A.; Miller, D.; Alemán, B. J. A Fast and Sensitive Room-Temperature Graphene Nanomechanical Bolometer. *Nat. Commun.* **2019**, *10*, 4726.

https://doi.org/10.1021/acsami.2c17477
ACS Appl. Mater. Interfaces XXXX, XXX, XXX−XXX